Eur. Phys. J. Plus (2018) **133**: 24
DOI 10.1140/epjp/i2018-11844-0

THE EUROPEAN PHYSICAL JOURNAL PLUS

Regular Article

Cattaneo-Christov heat flux effect on hydromagnetic radiative Oldroyd-B liquid flow across a cone/wedge in the presence of cross-diffusion

M. Gnaneswara Reddy[a]

Department of Mathematics, Acharya Nagarjuna University Campus, Ongole - 523 001, India

Received: 1 April 2017 / Revised: 13 December 2017
Published online: 25 January 2018 –

Abstract. The present article scrutinizes the prominent characteristics of the Cattaneo-Christov heat flux on magnetohydrodynamic Oldroyd-B radiative liquid flow over two different geometries. The effects of cross-diffusion are considered in the modeling of species and energy equations. Similarity transformations are employed to transmute the governing flow, species and energy equations into a set of nonlinear ordinary differential equations (ODEs) with the appropriate boundary conditions. The final system of dimensionless equations is resolved numerically by utilizing the R-K–Fehlberg numerical approach. The behaviors of all physical pertinent flow controlling variables on the three flow distributions are analyzed through plots. The obtained numerical results have been compared with earlier published work and reveal good agreement. The Deborah numbers γ_1 and γ_2 have quite opposite effects on velocity and energy fields. The increase in thermal relaxation parameter β corresponds to a decrease in the fluid temperature. This study has salient applications in heat and mass transfer manufacturing system processing for energy conversion.

1 Introduction

In recent years, the phenomenon of heat transfer has attracted interest due to its applications in industrial and manufacturing engineering, cooling of nuclear reactors, heat conduction in pumps, production of energy. Fourier [1] initially reported the basic heat conduction law and features of heat transfer. Subsequently, some modification in Fourier's law of heat conduction, which includes the additional term of relaxation time of energy flux, has been described by Cattaneo [2]. Christov [3] has modified the Cattaneo model [2] by considering energy relaxation time through Oldroyd upper-convected derivative and this is called the Cattaneo-Christov energy flux theory. The Cattaneo-Christov heat flux model applied to the flow of an incompressible liquid has been examined by Tibullo and Zampoli [4]. Khan *et al.* [5] explored the numerical analysis of the Cattaneo-Christov heat flux on the viscoelastic liquid flow along an exponentially sheet. Shehzad *et al.* [6] studied the mathematical simulation for the Cattaneo-Christov heat flux of a third-grade fluid. Cattaneo-Christov heat flux and partial slip flow in a viscoelastic liquid past a moving sheet was analyzed by Han *et al.* [7]. Recently, Gnaneswara Reddy and Rama Subba Reddy [8] examined the viscous dissipation and the Cattaneo-Christov heat flux effects on the polar fluid across a nonlinear stretching vertical surface. From this study, they found that the thermal relaxation time is efficient in reducing the dimensionless liquid temperature.

The phenomenon of thermal radiation has received prominent interest in the heat transfer mechanism due to its broad range of applications, which include nuclear power plants, the design of reliable equipment in manufacturing industries, propulsion gas turbines and assorted aircraft production, satellites, missiles and space launching vehicles. Thermal radiative flows in the presence of a magnetic field at high temperature can be found in solar power technology, electrical power generation, geophysical flows, nuclear propulsion engineering. Boundary layer flow and the impact of energy radiation through various geometries and aspects for the Newtonian and non-Newtonian liquids were investigated by many researchers [9–18].

The study of heat and mass transfer fluid flows has considerable importance because of its numerous applications, such as in petroleum reservoirs, geothermal processes, nuclear catalytic reactors, etc. The impacts of cross-diffusion, such as diffusion-thermo effects (Dufour) and thermal-diffusion effects (Soret) become very notable when the concentration and temperature gradients are high, thus leading to second-order phenomena of liquids. In view of the

[a] e-mail: mgrmaths@gmail.com

above-mentioned crucial applications, some researchers [19–35] considered the effects of heat and mass transfer flow with different aspects and varied conditions in the presence of Dufour and Soret effects.

Researchers, engineers and scientists have concentrated on exploring the nature of non-Newtonian materials, which are very complex and complicated, because it is very difficult to expand a single constitutive relationship model to forecast the properties of these materials. Some of these non-Newtonian fluids are Oldroyd-B fluid, Maxwell fluid, Carreau and Walters-B fluids. Hayat *et al.* [36] analyzed the second-grade liquid in a porous channel with magnetic field. The MHD peristaltic flow of a Walters-B fluid in the presence of slip conditions was explored by Makinde *et al.* [37]. Many studies on Oldroyd-B liquid flows were performed with varied conditions and dimensions [38–49]. Shehzad *et al.* [50] examined the impact of mass transport and radiation on the 3D flow of an Oldroyd-B fluid. Very recently, an analysis of the hydromagnetic flow of an Oldroyd-B liquid was examined by Hayat *et al.* [51], which revealed that the retardation time and fluid relaxation constants have opposite behaviors on the dimensionless axial velocity and concentration profiles. Sandeep and Gnaneswara Reddy [52] presented the cross-diffusion effects and double stratification on the hydromagnetic Oldroyd-B liquid flow over a melting surface.

Inspired by the aforementioned applications and analyses, the objective of the current study is to examine the cross-diffusion effects on the hydromagnetic radiative Oldroyd-B liquid flow through a cone/wedge in the presence of Cattaneo-Christove heat flux. The governing flow equations along related conditions are converted into a BVP problem of ODEs by employing similarity transformation. The resultant transformed differential equations with flow conditions are resolved by the R-K–Fehlberg numerical procedure. The influence of several embedded flow controlling variables on the flow, thermal and species boundary layers is analyzed through plots and tables.

2 Model development and formulation

Consider a two-dimensional (2D) viscous and an incompressible laminar boundary layer time-independent flow in two distinct geometries (cone and wedge). Thermal radiation and Cattaneo-Christov heat flux effects are introduced. The effects of cross-diffusion are included in the species and energy equations. The geometry of the flow problem is shown in fig. 1. A uniform transverse magnetic field of strength B_0 is applied in the vertical direction of the flow surface of the cone/wedge. Let us suppose that r is the cone radius and α is the half angle of the cone/wedge. The temperature $T_w = T_\infty + ax^s$ and concentration $C_w = C_\infty + bx^q$ are maintained near the surface. It is supposed that the magnetic Reynolds number is small and, therefore, the induced magnetic field is less as compared to the externally applied magnetic field. In view of the above suppositions, the flow governing equations reporting the physical model are

$$\frac{\partial}{\partial x}\left(r^m\frac{\partial \xi}{\partial y}\right) - \frac{\partial}{\partial y}\left(r^m\frac{\partial \xi}{\partial x}\right) = 0, \tag{1}$$

$$\frac{\partial \xi}{\partial y}\frac{\partial^2 \xi}{\partial x \partial y} - \frac{\partial \xi}{\partial x}\frac{\partial^2 \xi}{\partial y^2} + \lambda_1\left(\left(\frac{\partial \xi}{\partial y}\right)^2\frac{\partial^3 \xi}{\partial x^2 \partial y} - \left(\frac{\partial \xi}{\partial x}\right)^2\frac{\partial^3 \xi}{\partial y^3} - 2\frac{\partial \xi}{\partial y}\frac{\partial \xi}{\partial x}\frac{\partial^3 \xi}{\partial x \partial y^2}\right) = \left(\beta_T(T - T_\infty) + \beta_C(C - C_\infty)\right) g\cos\alpha$$
$$+ \upsilon\left(\frac{\partial^3 \xi}{\partial y^3} + \lambda_2\left(\frac{\partial \xi}{\partial y}\frac{\partial^4 \xi}{\partial x \partial y^3} - \frac{\partial \xi}{\partial x}\frac{\partial^4 \xi}{\partial y^4} - \frac{\partial^2 \xi}{\partial x \partial y}\frac{\partial^3 \xi}{\partial y^3} + \frac{\partial^2 \xi}{\partial y^2}\frac{\partial^3 \xi}{\partial x \partial y^2}\right)\right) - \frac{\sigma B_0^2}{\rho}\frac{\partial \xi}{\partial y}, \tag{2}$$

$$\frac{\partial \xi}{\partial y}\frac{\partial T}{\partial x} - \frac{\partial \xi}{\partial x}\frac{\partial T}{\partial y} + \delta\left(\frac{\partial \xi}{\partial y}\left(\frac{\partial^2 \xi}{\partial x \partial y}\frac{\partial T}{\partial x} - 2\frac{\partial \xi}{\partial x}\frac{\partial^2 T}{\partial x \partial y}\right) + \left(\frac{\partial \xi}{\partial x}\right)^2\frac{\partial^2 T}{\partial y^2} + \frac{\partial \xi}{\partial x}\left(\frac{\partial^2 \xi}{\partial y \partial x}\frac{\partial T}{\partial y} - \frac{\partial^2 \xi}{\partial y^2}\frac{\partial T}{\partial x}\right) + \left(\frac{\partial \xi}{\partial y}\right)^2\frac{\partial^2 T}{\partial x^2}\right) =$$
$$\frac{k}{\rho c_p}\frac{\partial^2 T}{\partial y^2} - \frac{1}{\rho c_p}\frac{\partial q_r}{\partial y} + \frac{D_m k_T}{c_s c_p}\frac{\partial^2 C}{\partial y^2}, \tag{3}$$

$$\frac{\partial \xi}{\partial y}\frac{\partial C}{\partial x} - \frac{\partial \xi}{\partial x}\frac{\partial C}{\partial y} = D_m\frac{\partial^2 C}{\partial y^2} + \frac{D_m k_T}{T_m}\frac{\partial^2 T}{\partial y^2}. \tag{4}$$

The associate initial and boundary conditions are

$$\begin{aligned} &u = u_w = \upsilon x/l^2, \quad v = v_w, \quad T = T_w = T_\infty + ax^s, \quad C = C_w = C_\infty + bx^q, \quad \text{at} \quad y = 0, \\ &u \to 0, \quad T \to T_\infty, \quad C \to C_\infty, \quad \text{as} \quad y \to \infty. \end{aligned} \tag{5}$$

The suggested problem exhibits two distinct geometries, which are based on the following suppositions:

a) the flow is generated by a wedge ($m = 0$ and $\alpha \neq 0$);
b) the flow is generated by a cone ($m = 1$ and $\alpha \neq 0$);

where the velocity components across the x- and y-directions are u and v, respectively, a, b are constants, s, q are the temperature and concentration parameters, T_∞ and C_∞ are the ambient temperature and concentration, σ is the

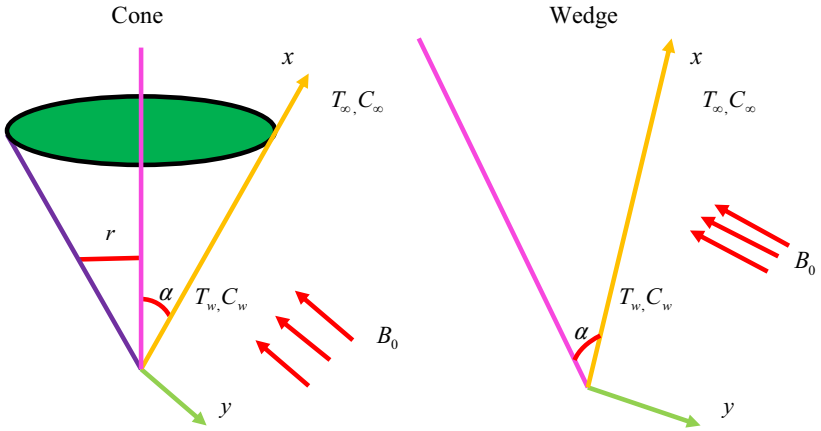

Fig. 1. Physical model of the problem.

electrical conductivity, υ is the viscosity (kinematic) of the fluid, B_0 is the applied magnetic field strength, g is the gravitational acceleration, ρ is the fluid density, β_T and β_C are the volumetric thermal and concentration expansion coefficients, δ is the relaxation time of heat flux, k is the thermal conductivity, q_r is the radiative heat flux, c_p is the heat capacitance, c_s is the concentration, D_m is the mass diffusivity coefficient, k_T is the thermal diffusion ratio, l is the characteristic length.

The radiative energy flux q_r is imposed according to the Rosseland approximation for thermal radiation [53] as

$$q_r = -\frac{4\sigma^*}{3k^*}\frac{\partial T^4}{\partial y}, \tag{6}$$

where k^* is the mean absorption coefficient and σ^* is the Stefan-Boltzmann constant.

It is considered that the temperature differences within the flow are sufficiently low and hence the term T^4 can be expressed as the linear function of the temperature about T_∞ and, omitting higher-order terms, we have

$$T^4 \cong 4T_\infty^3 T - 3T_\infty^4. \tag{7}$$

We introduce the following similarity transformations:

$$\zeta = yl^{-1}, \quad u = \upsilon x l^{-2} f'(\zeta), \quad v = -\upsilon(m+1)l^{-1}f(\zeta), \quad T = T_\infty + ax^s\theta(\zeta), \quad C = C_\infty + bx^q\phi(\zeta). \tag{8}$$

Utilizing eqs. (6), (7) and (8) in eqs. (2)–(5), we obtain

$$\frac{\partial^3 f}{\partial\zeta^3} + (m+1)f\frac{\partial^2 f}{\partial\zeta^2} - \left(\frac{\partial f}{\partial\zeta}\right)^2 + \gamma_1(m+1)\left(2(m+1)f\frac{\partial f}{\partial\xi}\frac{\partial^2 f}{\partial\zeta^2} - f^2\frac{\partial^3 f}{\partial\zeta^3}\right)$$
$$+\gamma_2\left(\frac{\partial^2 f}{\partial\zeta^2}^2 - (m+1)f\frac{\partial^4 f}{\partial\zeta^4}\right) - M\frac{\partial f}{\partial\zeta} + (Gr\theta + Gc\phi)\cos\alpha = 0, \tag{9}$$

$$\left(1+\frac{4}{3}Ra\right)\frac{\partial^2\theta}{\partial\zeta^2} - \Pr\beta\left[\left(s\left(\frac{\partial f}{\partial\zeta}\right)^2 - (m+1)f\frac{\partial^2 f}{\partial\zeta^2}\right)s\theta + (m+1-2s)(m+1)f\frac{\partial f}{\partial\zeta}\frac{\partial\theta}{\partial\zeta} + f^2(m+1)^2\frac{\partial^2\theta}{\partial\zeta^2}\right]$$
$$+Df\frac{\partial^2\phi}{\partial\zeta^2} + \Pr\left((m+1)f\frac{\partial\theta}{\partial\zeta} - s\frac{\partial f}{\partial\zeta}\theta\right) = 0, \tag{10}$$

$$\frac{\partial^2\phi}{\partial\zeta^2} + Sc\left((m+1)f\frac{\partial\phi}{\partial\zeta} - q\frac{\partial f}{\partial\zeta}\phi\right) + Sr\frac{\partial^2\theta}{\partial\zeta^2} = 0 \tag{11}$$

and the dimensionless transformed boundary conditions are

$$f = S, \quad \frac{\partial f}{\partial\zeta} = 1, \quad \theta = 1, \quad \phi = 1, \quad \text{at} \quad \zeta = 0,$$
$$\frac{\partial f}{\partial\zeta} \to 0, \quad \theta \to 0, \quad \phi \to 0, \quad \text{as} \quad \zeta \to \infty, \tag{12}$$

Table 1. Comparison of the present results with those of [54] for the local Nusselt number $(-\theta'(0))$ for several values M when $\gamma_1 = \gamma_2 = 0 = Ra = f_w$.

M	Reddy *et al.* [54]		Present results	
	Cone	Wedge	Cone	Wedge
0.1	1.0082	1.3130	1.008215	1.313082
0.5	0.9854	1.2661	0.985405	1.266161
1.0	0.9597	1.2135	0.959724	1.213508
2.0	0.9166	1.1255	0.916676	1.125525

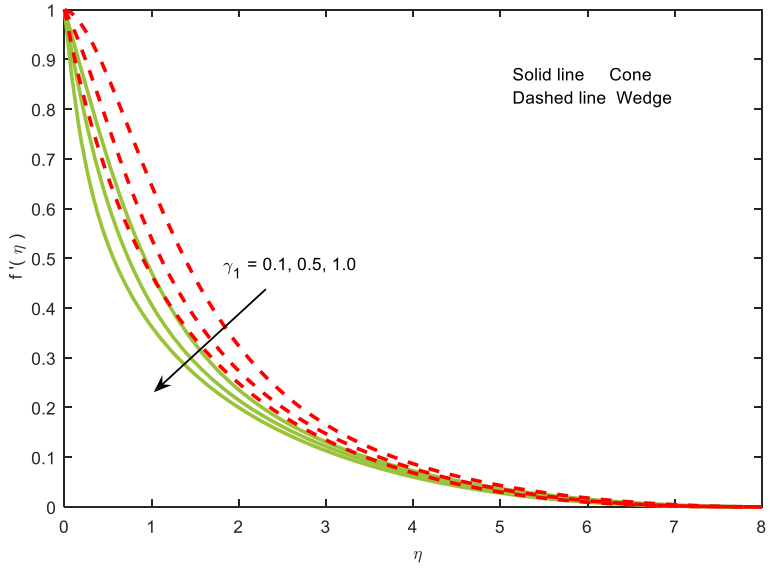

Fig. 2. Velocity curves for distinct values of γ_1.

in which $M = \frac{\sigma_0 B_0^2 l^2}{\rho \upsilon}$ is the magnetic field parameter, $Gr = \frac{l^2 g \beta_T (T_w - T_\infty)}{\upsilon u_w}$ is the energy Grashof number, $Gc = \frac{l^2 g \beta_T (C_w - C_\infty)}{\upsilon u_w}$ is the mass Grashof number, $\Pr = \frac{\mu c_p}{k}$ is the Prandtl number, $\beta = \frac{\delta \upsilon}{l^2}$ is the thermal relaxation parameter, $Ra = \frac{4\sigma^* T_\infty^3}{k k^*}$ is the radiation parameter, $Sr = \frac{D_m K_T (T_w - T_\infty)}{c_s c_p \upsilon (C_w - C_\infty)}$ is the Soret number, $Df = \frac{D_m K_T (C_w - C_\infty)}{c_s c_p \upsilon (T_w - T_\infty)}$ is the Dufour number, $S = \frac{-l v_w}{\upsilon (m+1)}$ is the suction parameter, and $Sc = \frac{\upsilon}{D_m}$ is the Schmidt number.

Due to the several physical applications, the dimensionless friction factor C_f, rate of heat transfer (Nusselt number Nu) and rate of mass transfer (Sherwood number Sh) are defined by

$$C_f = \left.\frac{\partial^2 f}{\partial \varsigma^2}\right|_{\varsigma=0}, \quad Nu = -\left.\frac{\partial \theta}{\partial \varsigma}\right|_{\varsigma=0}, \quad Sh = -\left.\frac{\partial \phi}{\partial \varsigma}\right|_{\varsigma=0}. \tag{13}$$

3 Results and discussion

The dimensionless flow governing equations (9)–(11) along the related boundary conditions (12) are numerically resolved by the R-K–Fehlberg integration technique. The main goal in this section is to scrutinize the physical characteristics of embedded variables on the three fields, such as dimensionless velocity, energy and concentration, respectively. The values of several variables are assumed for numerical computations: $Gc = Sr = s = q = 2.0$, $Gr = M = \alpha = \beta = Df = Ra = 0.5$, $\Pr = 0.7$, $S = 1$, $\gamma_1 = \gamma_2 = 0.2$, $Sc = 0.6$, and these values are kept fixed unless differently stated in figures and tables.

Table 1 is displayed for the comparison of the obtained numerical results with those of the existing literature on the heat transfer coefficient for assorted values of M. It is found that there is very good agreement with the obtained results. Therefore, this ensures accuracy and effectiveness of the present numerical method.

Behavior of the Deborah number γ_1 on the velocity $f'(\eta)$ and temperature $\theta(\eta)$ is sketched in figs. 2 and 3, respectively. From fig. 2, it is clear that increasing the values of γ_1 leads to a decrease in the fluid velocity and related

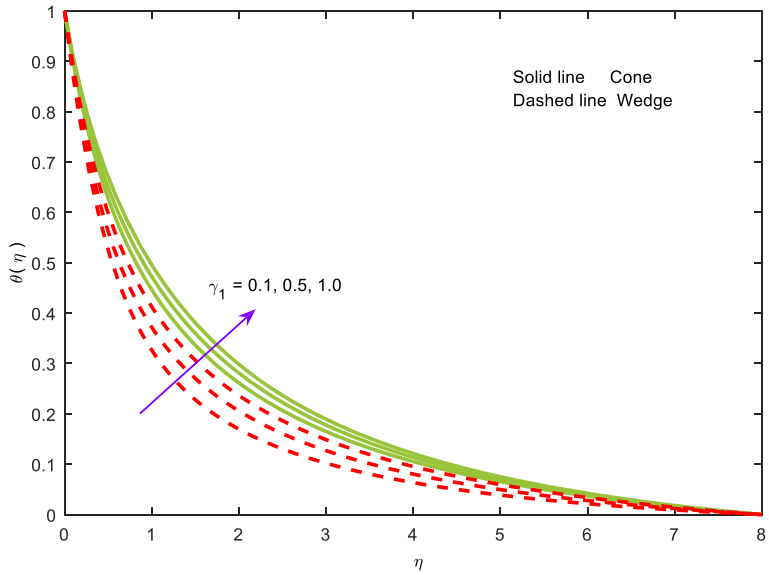

Fig. 3. Temperature curves for distinct values of γ_1.

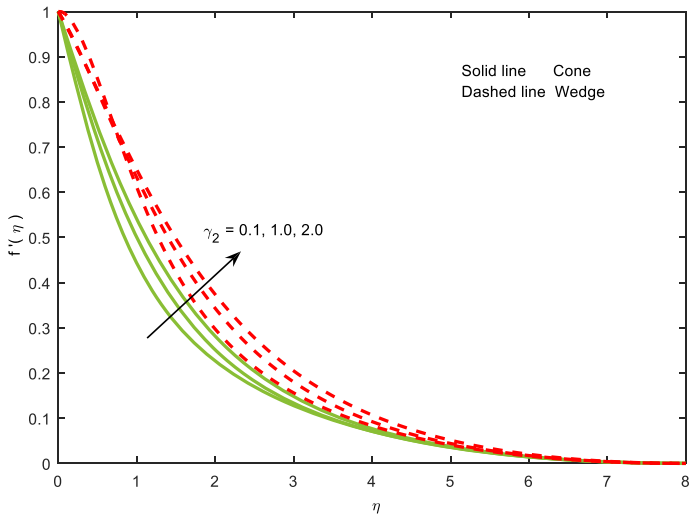

Fig. 4. Velocity curves for distinct values of γ_2.

thickness of the boundary layer. The liquid temperature increases to the higher values of γ_1, which is inferred from fig. 3. This is due to the fact that the Deborah number γ_1 is a function of the relaxation time and it is maximum for higher γ_1, decreasing the fluid velocity and increasing the temperature field. This result agrees with that of the published work of Hayat *et al.* [55]. The temperature is higher over the cone rather than over the wedge for the Deborah number γ_1. In addition, the effect of the Deborah number γ_1 on the velocity and on energy fields has opposite behavior.

The variations of the Deborah number with respect to retardation time γ_2 on the non-dimensional velocity and energy distribution are portrayed in figs. 4 and 5. The dimensionless velocity field increases with an increase in γ_2, which enhances the corresponding energy boundary layer thickness, while a reverse effect on the fluid temperature (fig. 5) is seen. It is also seen that the Deborah number γ_2 has small variations in the temperature over cone and wedge.

The characteristics of the magnetic parameter M on dimensionless velocity, energy and species fields are illustrated figs. 6–8. It is observed, from fig. 6, that the velocity function diminishes with increasing values of M. This is due to the fact that the Lorentz force acts as a resistance force and this force increases the frictional resistance opposing the liquid flow in the viscous boundary layer thickness. However, a reverse trend is seen for the temperature and concentration functions, which are shown in figs. 7 and 8, and these results agree with those of [9].

Figures 9 and 10 are plotted to show the influence of the Grashof number Gr on the velocity function $f'(\eta)$ and temperature profile $\theta(\eta)$. It is observed, from fig. 9, that the velocity of the Oldroyd-B fluid increases with increasing values of Gr, while the energy field decreases for increasing values of Gr, which is clear from fig. 10.

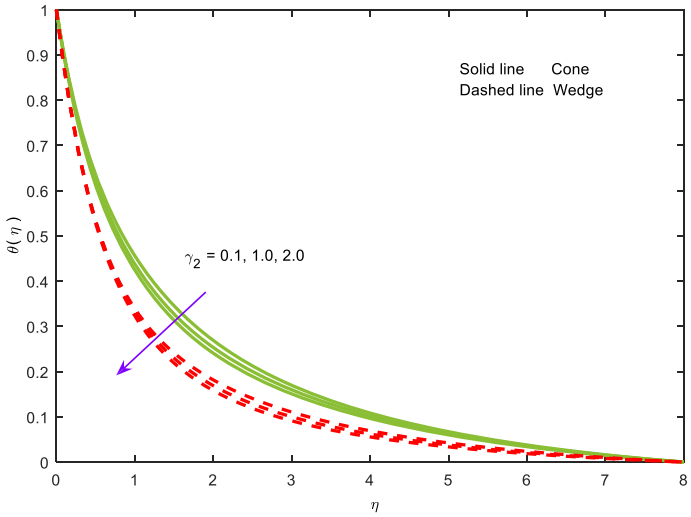

Fig. 5. Temperature curves for distinct values of γ_2.

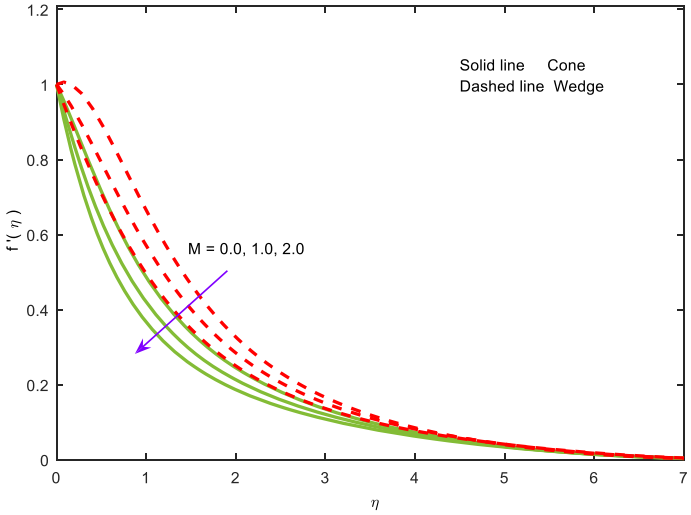

Fig. 6. Velocity curves for distinct values of M.

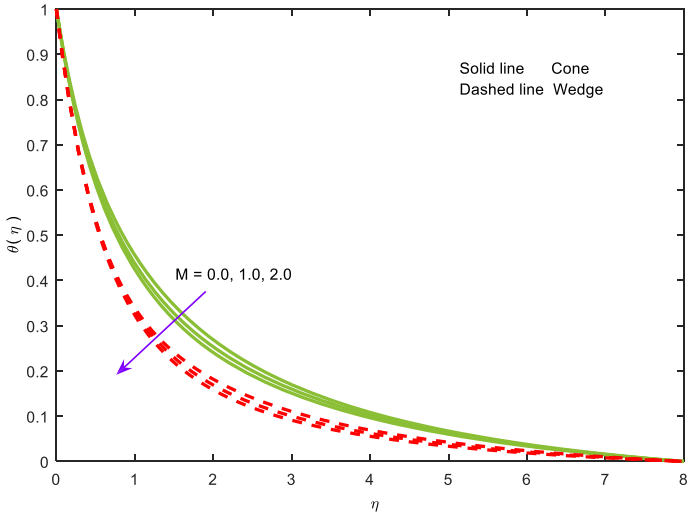

Fig. 7. Temperature curves for distinct values of M.

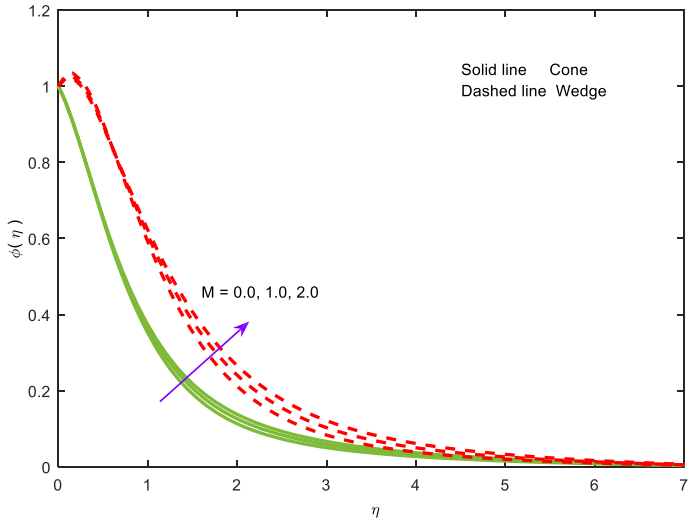

Fig. 8. Concentration curves for distinct values of M.

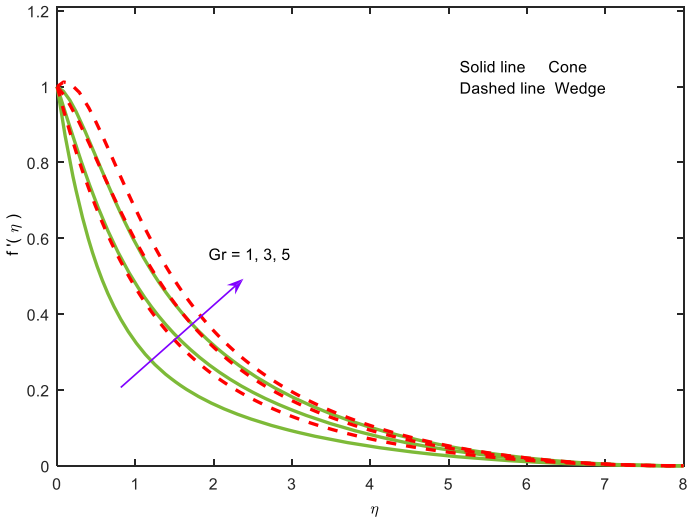

Fig. 9. Velocity curves for distinct values of Gr.

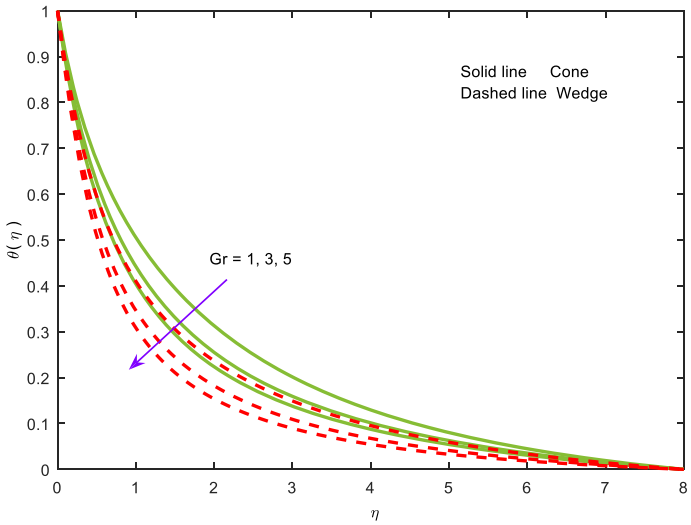

Fig. 10. Temperature curves for distinct values of Gr.

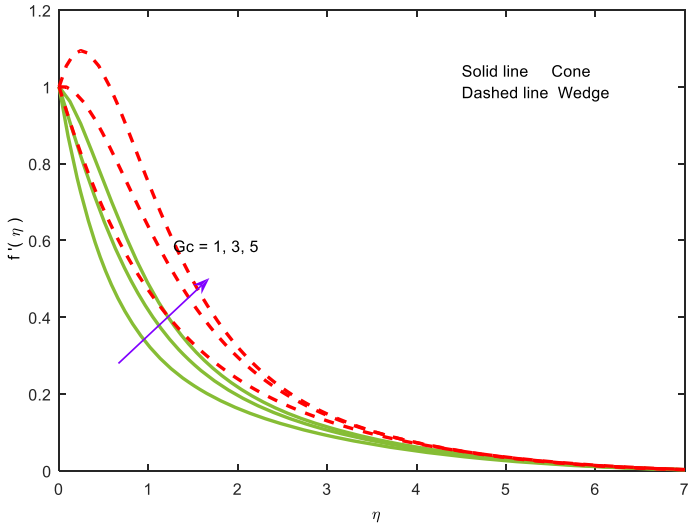

Fig. 11. Velocity curves for distinct values of Gc.

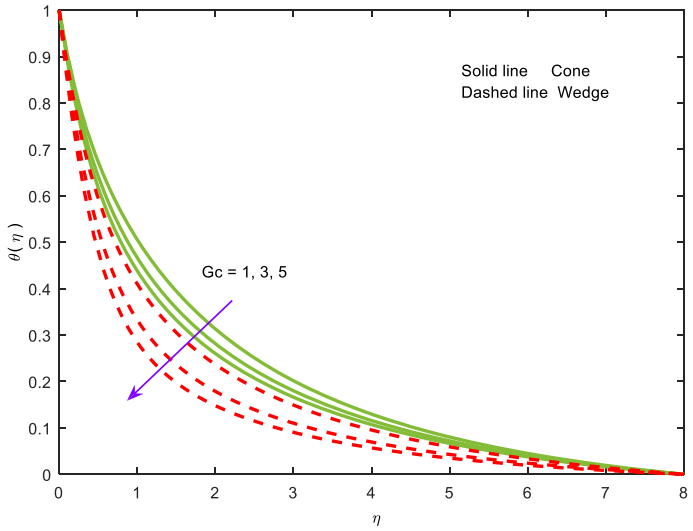

Fig. 12. Temperature curves for distinct values of Gc.

Furthermore, the temperature is more affected by the thermal Grashof number in the flow past a cone as compared to the flow across a wedge. Figures 11 and 12 are sketched for the impacts of mass/species Grashof number Gc on the velocity and dimensionless energy distribution $\theta(\eta)$. It is observed, from fig. 11, that the flow and the hydrodynamic boundary layer thickness are an increasing function of Gc, whereas opposite behavior is found for the temperature (see fig. 12.). Figure 13 shows the behavior of α on the axial velocity $f'(\eta)$, which reveals that the velocity diminishes for increasing values of α in both cone and wedge.

Figures 14–16 show the characteristics of the thermal radiation parameter Ra on the velocity $f'(\eta)$, $\theta(\eta)$ and concentration $\phi(\eta)$, respectively. It is observed, from figs. 14 and 15, that both the velocity and temperature functions increase for higher Ra, while an opposite effect is found for the dimensionless concentration function. Because of higher values of Ra additional heat is produced in the energy radiation process to the working liquid, which results in the improvement of fluid temperature. It may also be shown that the influence of Ra is a little stronger in the temperature over the cone than over the wedge. The results for the radiation on the three flow distributions have the same physical behavior as those of Pal and Mondal [11].

Figure 17 displays the influence of thermal relaxation parameter β on the temperature distribution function $\theta(\eta)$. It is quite evident from this figure that larger values of β decrease the temperature profile. It is clearly observed that an increase in β causes a decrease in the molecular heat, which diminishes the fluid flow temperature. It is further observed that the variations in dimensionless energy of the flow over the cone are notably superior to those over the wedge.

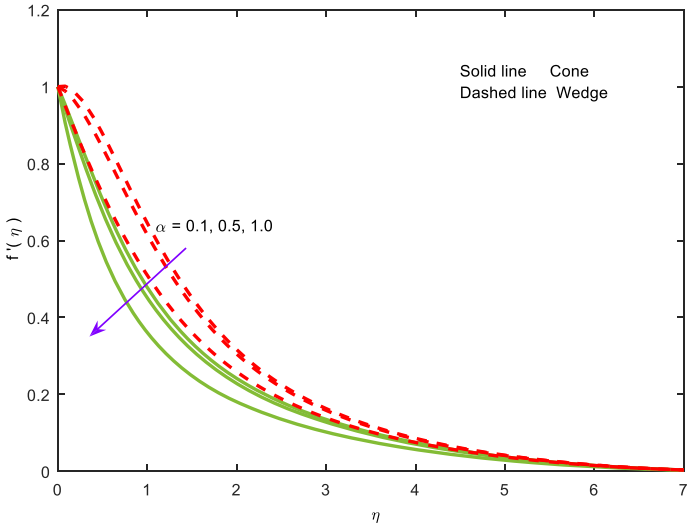

Fig. 13. Velocity curves for distinct values of α.

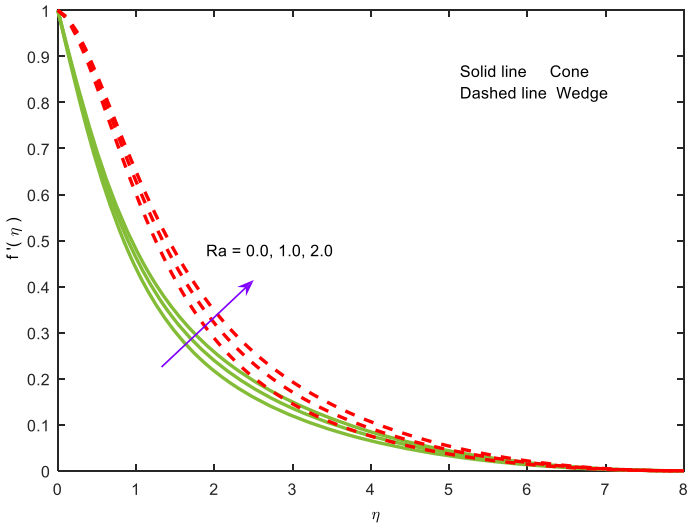

Fig. 14. Velocity curves for distinct values of Ra.

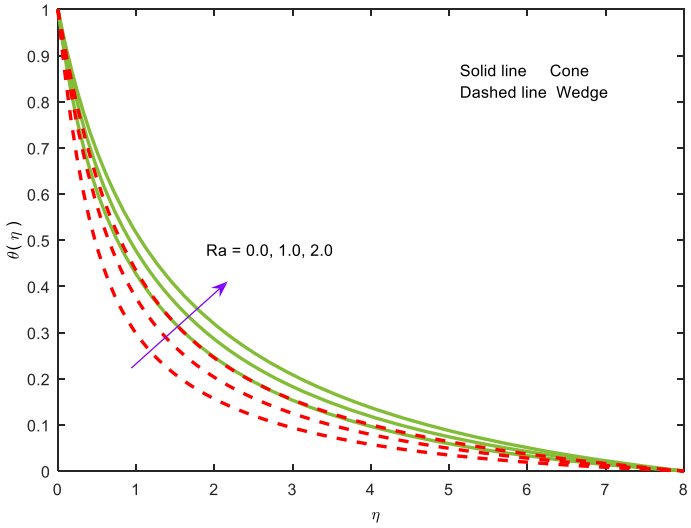

Fig. 15. Temperature curves for distinct values of Ra.

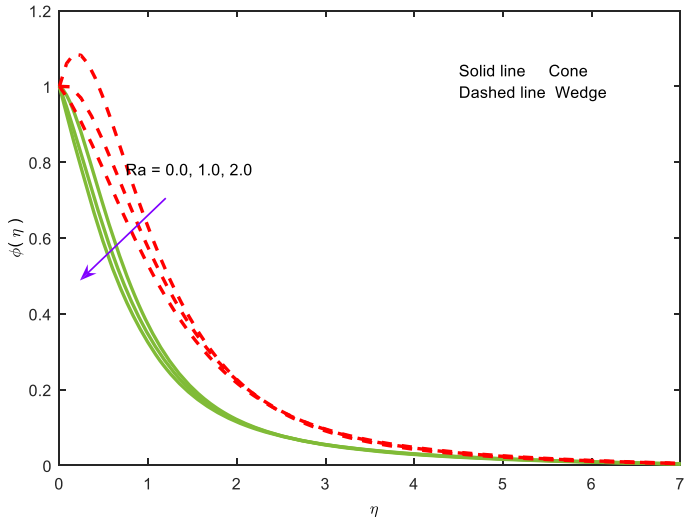

Fig. 16. Concentration curves for distinct values of Ra.

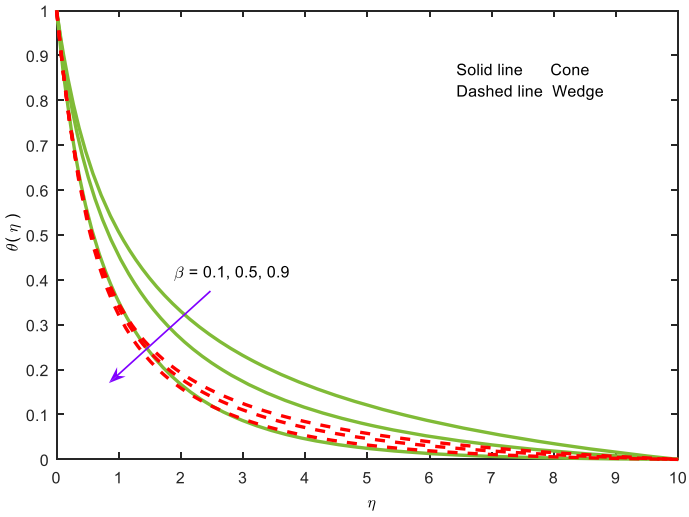

Fig. 17. Temperature curves for distinct values of β.

The variations in the curves of velocity, energy and concentration to the influence of the Soret number Sr are analyzed through figs. 18–20. From figs. 18 and 20, it is found that an increase in the Soret number Sr shows an increase in concentration and velocity and the related boundary layer thickness. But an opposite behavior appears in the case of dimensionless temperature and is evident from fig. 19. This is due to the fact that an increase in the Soret number Sr makes the energy diffusion of the material decrease, which is responsible for the reduction of the liquid temperature. This behavior coincides with the results of Gnaneswara Reddy and Bhaskar Reddy [26]. Furthermore, it is also seen that the liquid reaches maximum temperature over the cone than over the wedge.

The impact of the Dufour parameter Df on the velocity $f'(\eta)$, temperature function $\theta(\eta)$, and species profile $\phi(\eta)$ is shown in figs. 21–23, respectively. From figs. 21 and 22, it can be found that the velocity and fluid temperature enhance with increasing the values of Df and, significantly, the hydrodynamical and energy boundary layer thickness. The opposite effect on the dimensionless concentration function is observed from fig. 23. The curves of concentration increase near the cone compared to the wedge to the peak values of Df. Figure 24 shows that the dimensionless velocity $f'(\eta)$ is a decreasing function, for higher values, of the suction parameter S. The behavior of the variable wall temperature parameter s and concentration parameter q is illustrated in figs. 25 and 26. It can be observed from these plots that both liquid temperature and concentration reduce with increasing values of s and q.

The numerical values of the friction factor $(f''(0))$, Nusselt number $(-\theta'(0))$ and Sherwood number $(-\phi'(0))$ near the wall over the cone and wedge are displayed in tables 2–4 under the characteristics of embedded flow variables. It can be seen, from table 2, that the friction factor increases with increasing values of Gr, Gc, γ_2, β, Sr and Df, whereas the opposite happens for the flow variables, such as M, γ_1, and Ra. With higher values of Gr, Gc, γ_2, β, and Sr, the Nusselt number increases, but an opposite behavior is seen for dimensionless parameters M, γ_1, β, Ra and Df (see table 2).

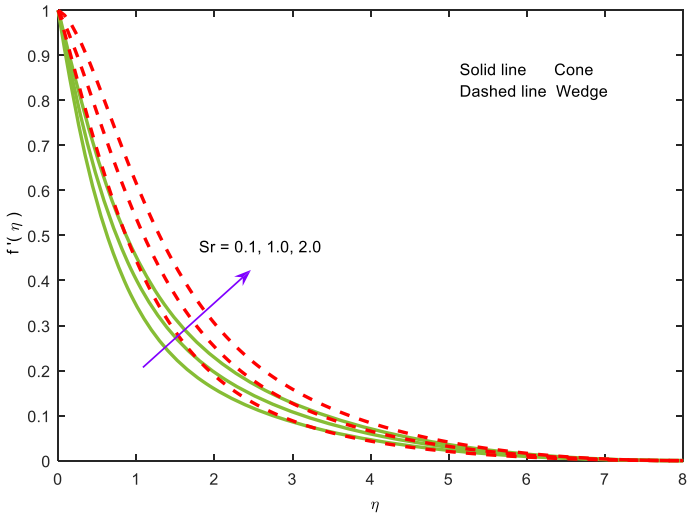

Fig. 18. Velocity curves for distinct values of Sr.

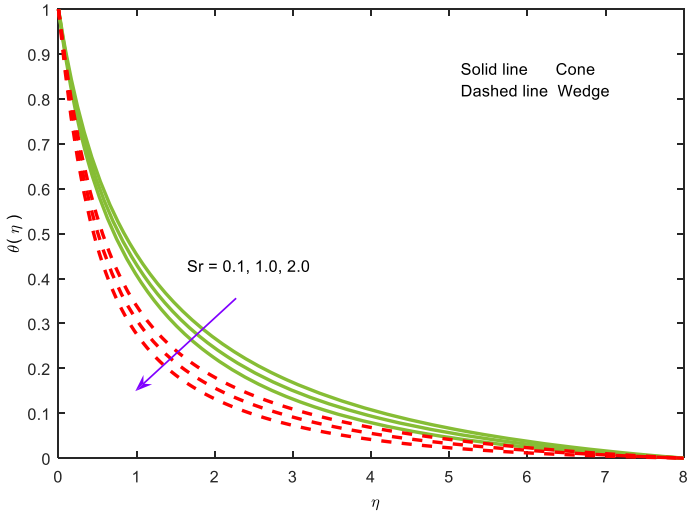

Fig. 19. Temperature curves for distinct values of Sr.

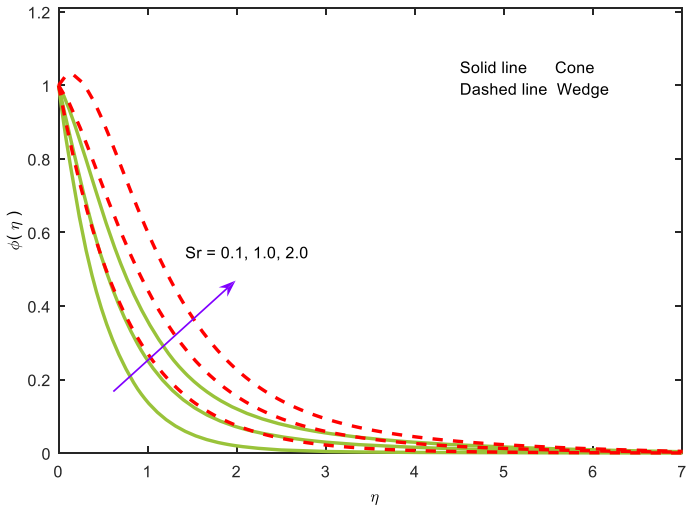

Fig. 20. Concentration curves for distinct values of Sr.

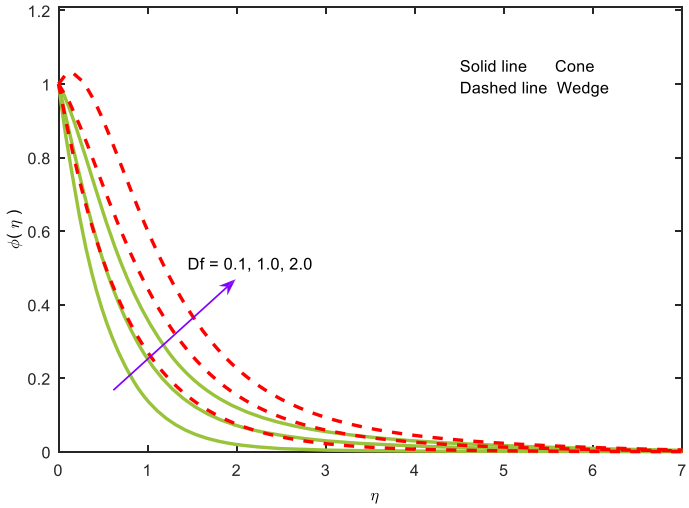

Fig. 21. Velocity curves for distinct values of Df.

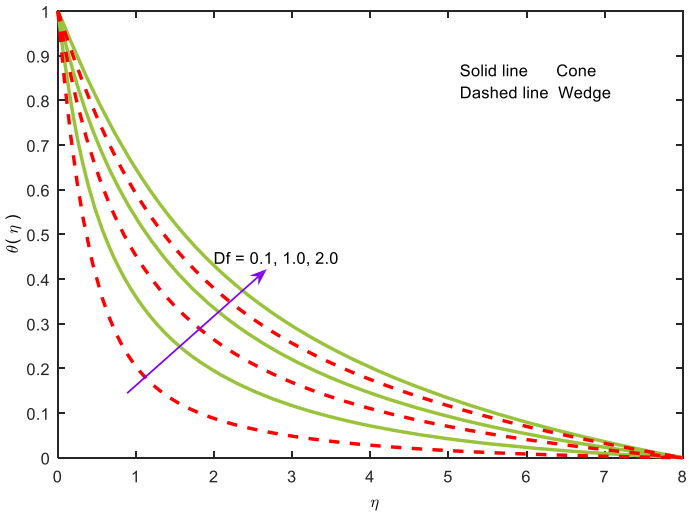

Fig. 22. Temperature curves for distinct values of Df.

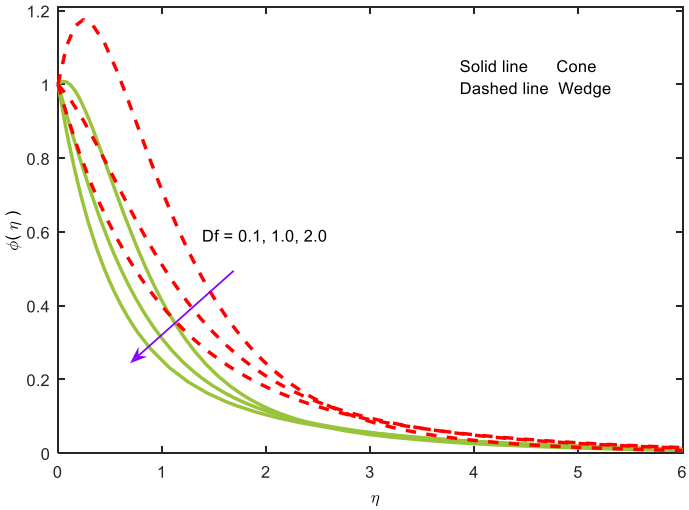

Fig. 23. Concentration curves for distinct values of Df.

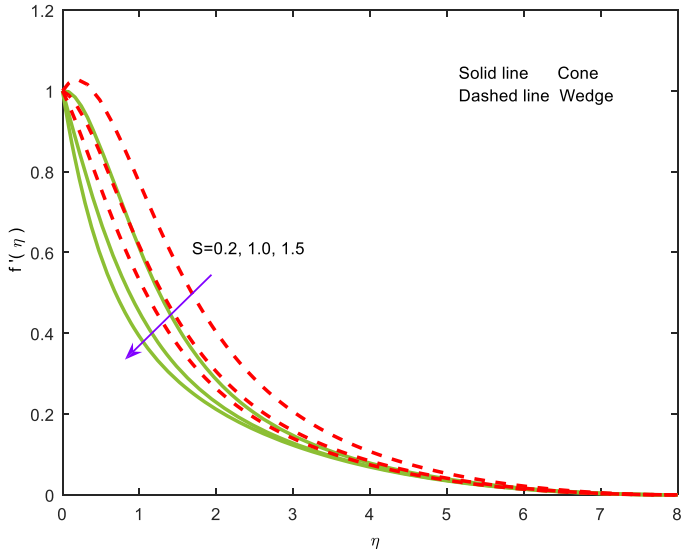

Fig. 24. Velocity curves for distinct values of S.

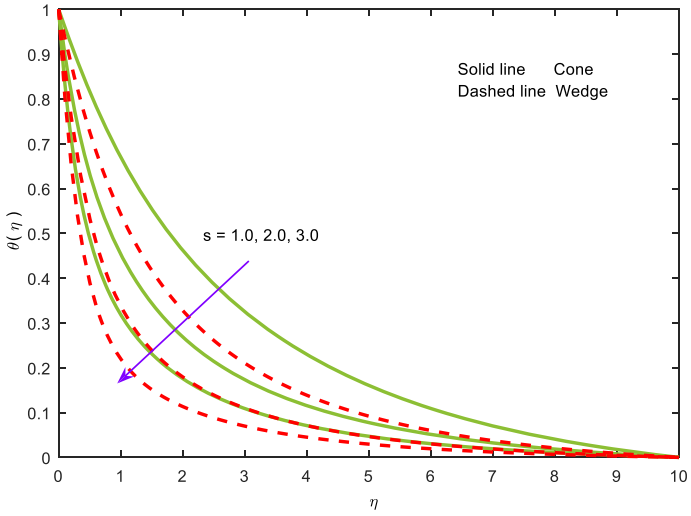

Fig. 25. Temperature curves for distinct values of s.

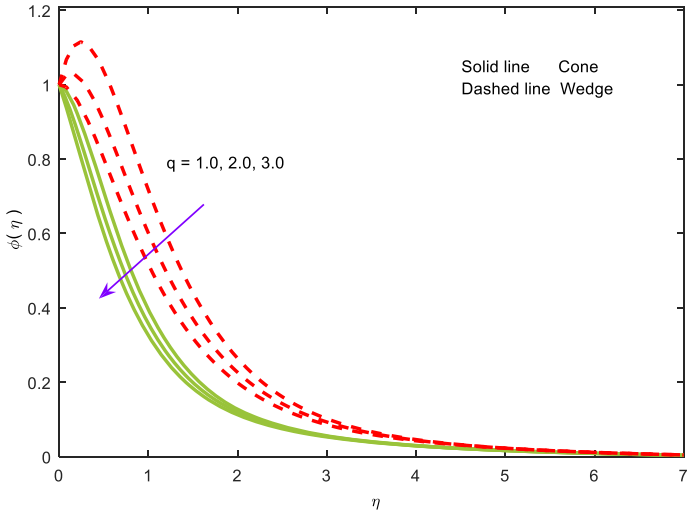

Fig. 26. Concentration curves for distinct values of q.

Table 2. Numerical values of skin-friction coefficient ($f''(0)$) to the flow in the cone and that in the wedge.

M	Gr	Gc	γ_1	γ_2	β	Ra	Sr	Df	Skin-friction coefficient	
									Cone	Wedge
0.5									−0.868005	−0.273988
1.0									−1.047456	−0.475857
2.0									−1.354790	−0.820201
	1.0								−1.253497	−0.573132
	2.0								−0.868005	−0.273988
	3.0								−0.527967	−0.007326
		1.0							−1.075243	−0.578909
		2.0							−0.868005	−0.273988
		3.0							−0.665738	0.022366
			0.1						−0.760542	−0.205721
			0.5						−1.251494	−0.552605
			1						−2.084570	−1.245752
				0.1					−0.913996	−0.196866
				0.5					−0.774907	−0.356257
				1					−0.685379	−0.385335
					0.2				−0.955316	−0.281400
					0.5				−0.868005	−0.273988
					0.9				−0.795587	−0.267552
						0.5			−0.868005	−0.273988
						1.0			−0.842600	−0.253935
						2.0			−0.799643	−0.220218
							0.5		−0.769079	−0.548964
							1.0		−1.018942	−0.470270
							2.0		−0.868005	−0.273988
								0.5	−0.868005	−0.273988
								1.0	−0.775015	−0.205991
								2.0	−0.651441	−0.115614

Table 3. Numerical values of the local Nusselt number $(-\theta'(0))$ to the flow in the cone and that in the wedge.

M	Gr	Gc	γ_1	γ_2	β	Ra	Sr	Df	Nusselt number	
									Cone	Wedge
0.5									0.985373	1.266055
1.0									0.959702	1.213527
2.0									0.916599	1.125537
	1.0								0.920109	1.184997
	2.0								0.985373	1.266055
	3.0								1.036673	1.329905
		1.0							0.964741	1.203756
		2.0							0.985373	1.266055
		3.0							1.004859	1.323100
			0.1						0.999417	1.294440
			0.5						0.947439	1.187710
			1						0.897407	1.085268
				0.1					0.978393	1.267183
				0.5					1.001691	1.271227
				1					1.021330	1.284583
					0.2				1.133105	1.237807
					0.5				0.985373	1.266055
					0.9				0.895006	1.301601
						0.5			0.985373	1.266055
						1.0			0.888651	1.099616
						2.0			0.753653	0.889955
							0.5		1.094251	1.477073
							1.0		1.070473	1.425278
							2.0		0.985373	1.266055
								0.5	0.985373	1.266055
								1.0	0.608290	0.809696
								2.0	0.162174	0.347503

Table 4. Numerical values of the local Sherwood number $(-\phi'(0))$ to the flow in the cone and that in the wedge.

M	Gr	Gc	γ_1	γ_2	β	Ra	Sr	Df	Sherwood number	
									Cone	Wedge
0.5									1.505918	0.369637
1.0									1.502883	0.394098
2.0									1.496138	0.433068
	1.0								1.500283	0.407859
	2.0								1.505918	0.369637
	3.0								1.508818	0.338409
		1.0							1.501222	0.397651
		2.0							1.505918	0.369637
		3.0							1.510030	0.342657
			0.1						1.508264	0.356437
			0.5						1.496318	0.404585
			1						1.476425	0.447815
				0.1					1.504265	0.368832
				0.5					1.508499	0.367303
				1					1.509642	0.360655
					0.2				1.232575	0.424657
					0.5				1.505918	0.369637
					0.9				1.668817	0.302140
						0.5			1.505918	0.369637
						1.0			1.682038	0.662092
						2.0			1.924237	1.020503
							0.5		2.062547	1.426702
							1.0		2.070006	1.009664
							2.0		1.505918	0.369637
								0.5	1.505918	0.369637
								1.0	2.187275	1.154678
								2.0	2.978708	1.920941

Finally, the Sherwood number increases for larger values of the variables Gr, Gc, γ_2, β, Ra and Df, while a reverse behavior is seen for the flow variables M, γ_1, and Sr. Furthermore, a preferable heat transfer production can be obtained on the flow over the wedge as compared to that over the cone.

4 Concluding remarks

The influence of the Cattaneo-Christov heat flux on a hydromgnatic Oldroyd-B radiative liquid flow across two different geometries in the presence of cross-diffusion has been investigated. The described problem has been modeled and the partial differential equations (PDEs) are reduced into ordinary differential equations (ODEs) by employing suitable similarity transformations. The resulting equations are resolved numerically by Runge-Kutta–Fehlberg algorithm with shooting scheme. The key observations for the current study are listed as follows:

1) The magnetic parameter M reduces the dimensionless velocity and the related boundary layer thickness.
2) The impact of the Deborah numbers, γ_1 and γ_2, on the velocity and liquid temperature is opposite.
3) The thermal radiation parameter Ra has a dominant effect on the fluid temperature field across the cone compared to that across the wedge.
4) The thickness of the thermal boundary layer and temperature decrease for larger values of species and thermal buoyancy parameters.
5) The fluid temperature $\theta(\eta)$ reduces with increasing values of thermal relaxation time β.
6) The Nusselt number is high over the wedge with the cone for the larger thermal radiation while the opposite influences on the Sherwood number.

Nomenclature

a, b	Constants	Ra	Radiation parameter
B_0	Applied magnetic field strength	s	Temperature parameter of the wall
c_p	Heat capacitance	Sr	Soret number
c_s	Concentration	S	Suction parameter
C_∞	Ambient concentration	Sc	Schmidt number
C_w	Concentration near the surface	T_w	Temperature near the surface
D_m	Mass diffusivity coefficient	T_∞	Ambient temperature
Df	Dufour number	u	Velocity component along x
Gr	Grashof number in temperature	v	Velocity component along y
Gc	Grashof number in concentration	α	Half angle of the wedge/cone
g	Gravitational acceleration	β	Thermal relaxation parameter
k	Thermal conductivity	β_T	Volumetric thermal expansion coefficient
k^*	Mean absorption coefficient	β_C	Volumetric concentration expansion coefficient
k_T	Thermal diffusion ratio	γ_1	Deborah number with respect to relaxation time
l	Characteristic length	γ_2	Deborah number with respect to retardation time
M	Magnetic field parameter	υ	Viscosity (kinematic) of the fluid
Pr	Prandtl number,	σ	Electrical conductivity
q	Concentration parameter of the wall	σ^*	Stefan-Boltzmann constant
q_r	Radiative heat flux	ρ	Fluid density
r	Radius of the cone	δ	Relaxation time of heat flux

References

1. J.B.J. Fourier, *Théorie analytique de la chaleur* (Paris, 1822).
2. C. Cattaneo, Atti Semin. Mat. Fis. Univ. Modena Reggio Emilia **3**, 83 (1948).
3. C.I. Christov, Mech. Res. Commun. **36**, 481 (2009).
4. V. Tibullo, V. Zampoli, Mech. Res. Commun. **38**, 77 (2011).
5. J.A. Khan, M. Mustafa, T. Hayat, A. Alsaedi, PLoS ONE **10**, e0137363 (2015).
6. S.A. Shehzad, F.M. Abbasi, T. Hayat, B. Ahmad, Appl. Math. Mech. **37**, 761 (2016).

7. S. Han, L. Zheng, C. Li, X. Zhang, Appl. Math. Lett. **38**, 87 (2014).
8. M. Gnaneswara Reddy, G. Rama Subba Reddy, Front. Heat Mass Transf. (2017) https://doi.org/10.5098/hmt.8.20.
9. A.J. Chamkha, M. Mujtaba, A. Quadri, C. Issa, Heat Mass Transfer **39**, 305 (2003).
10. O.D. Makinde, A. Ogulu, Chem. Eng. Commun. **195**, 1575 (2008).
11. D. Pal, H. Mondal, Meccanica **44**, 133 (2009).
12. T. Hayat, Z. Abbas, I. Pop, S. Asghar, Int. J. Heat Mass Transfer **53**, 466 (2010).
13. T. Hayat, M. Qasim, Z. Abbas, Z. Naturforsch. A **65**, 231 (2010).
14. T. Hayat, M. Qasim, Int. J. Heat Mass Transfer **53**, 4780 (2010).
15. T. Hayat, R. Sajjad, Z. Abbas, M. Sajid, A.A. Hendi, Int. J. Heat Mass Transfer **54**, 854 (2011).
16. M. Gnaneswara Reddy, Ain Shams Eng. J. **5**, 169 (2014).
17. T. Hayat, A. Shafiq, A. Alsaedi, PLoS ONE **9**, e83153 (2014).
18. M. Gnaneswara Reddy, Eur. Phys. J. Plus **129**, 41 (2014).
19. M.S. Alam, M.M. Rahman, M.A. Samad, Nonlinear Anal. **11**, 217 (2006).
20. M.K. Partha, P.V.S.N. Murthy, G.P. Raja Sekhar, J. Heat Transf. **128**, 605 (2006).
21. A. Postelnicu, Heat Mass Transf. **43**, 595 (2006).
22. A. Mahdy, Int. Commun. Heat Mass Transf. **36**, 1067 (2009).
23. C.Y. Cheng, Int. Commun. Heat Mass Transf. **36**, 1020 (2009).
24. A. Mahdy, J. Non-Newtonian Fluid Mech. **165**, 568 (2010).
25. T. Hayat, M. Mustafa, I. Pop, Commun. Nonlinear Sci. Numer. Simul. **15**, 1183 (2010).
26. M. Gnaneswara Reddy, N. Bhaskar Reddy, Int. J. Appl. Math Mech. **6**, 1 (2010).
27. O.D. Makinde, Lat. Am. Appl. Res. **41**, 63 (2011).
28. P.S. Reddy, V.P. Rao, J. Appl. Fluid Mech. **5**, 139 (2012).
29. A.J. Chamkha, A.M. Rashad, Can. J. Chem. Eng. (2014) https://doi.org/10.1002/cjce.21894.
30. M. Gnaneswara Reddy, Alex. Eng. J. **55**, 1225 (2016).
31. M. Gnaneswara Reddy, O.D. Makinde, J. Mol. Liq. **223**, 1242 (2016).
32. M. Gnaneswara Reddy, N. Sandeep, Ain Shams Eng. J. (2016) https://doi.org/10.1016/j.asej.2016.06.012.
33. M. Bilal Ashraf, T. Hayat, A. Alsaedi, S.A. Shehzad, Results Phys. **6**, 917 (2016).
34. T. Hayat, S. Farooq, A. Alsaedi, B. Ahmad, Int. J. Therm. Sci. **112**, 68 (2017).
35. M. Gnaneswara Reddy, N. Sandeep, J. Comput. Appl. Res. Mech. Eng. **7**, 1 (2017).
36. T. Hayat, Y. Wang, K. Hutter, S. Asghar, A.M. Siddiqui, Math. Prob. Eng. **4**, 347 (2004).
37. O.D. Makinde, M. Gnaneswara Reddy, K. Venugopal Reddy, J. Appl. Fluid Mech. **10**, 1105 (2017).
38. L. Zheng, Y. Liu, X. Zhang, Math. Comput. Model. **54**, 780 (2011).
39. T. Hayat, Masood Khan, M. Ayub, Appl. Math. Comput. **151**, 105 (2004).
40. T. Hayat, S.A. Shehzad, M. Mustafa, A.A. Hendi, Int. J. Chem. Reactor Eng. (2012) https://doi.org/10.1515/1542-6580.2655.
41. S. Abbasbandy, T. Hayat, A. Alsaedi, M.M. Rashidi, Int. J. Numer. Methods Heat Fluid Flow **24**, 390 (2014).
42. S.S. Motsa, Z.G. Makukula, S. Shateyi, PLoS ONE **10**, e0133507 (2015).
43. T. Hayat, T. Muhammad, S.A. Shehzad, M.S. Alhuthali, J. Lu, J. Mol. Liq. **212**, 272 (2015).
44. T. Hayat, M. Imtiaz, A. Alsaedi, Appl. Math. Mech. **37**, 573 (2016).
45. T. Hayat, S. Qayyum, A. Alsaedi, M. Waqa, J. Mol. Liq. **224**, 811 (2016).
46. S.A. Shehzad, F.M. Abbasi, T. Hayat, A. Alsaed, J. Mol. Liq. **224**, 274 (2016).
47. N. Ali, K. Javid, M. Sajid, A. Zaman, T. Hayat, Int. J. Heat Mass Transfer **94**, 500 (2016).
48. T. Hayat, T. Ayub, T. Muhammad, A. Alsaedi, J. Mol Liq. **234**, 9 (2017).
49. T. Hayat, Naveed Ahmed, M. Sajid, S. Asghar, Comput. Math. Appl. **54**, 407 (2007).
50. S.A. Shehzad, A. Alsaedi, T. Hayat, M.S. Alhuthali, J. Taiwan Inst. Chem. Eng. **45**, 787 (2014).
51. T. Hayat, M. Imtiaz, A. Alsaedi, S. Almezal, J. Magn. & Magn. Mater. **401**, 296 (2016).
52. N. Sandeep, M. Gnaneswara Reddy, Eur. Phys. J. Plus **132**, 147 (2017).
53. M.Q. Brewster, *Thermal Radiative Transfer and Properties* (John Wiley & Sons, 1992).
54. J.V. Ramana Reddy, V. Sugunamma, N. Sandeep, J. Mol. Liq. **223**, 1234 (2016).
55. T. Hayat, M. Imtiaz, A. Alsaedi, Appl. Math. Mech. **37**, 573 (2016).